Downloaded from orbit.dtu.dk on: Apr 18, 2024

DTU Library

Multi-stage generation of extreme ultraviolet dispersive waves by tapering gas-filled hollow-core anti-resonant fibers

Selim Habib, M. D.; Markos, Christos; Enrique Antonio-Lopez, J.; Correa, Rodrigo Amezcua; Bang, Ole; Bache, Morten

Published in:
Optics Express

Link to article, DOI:
10.1364/OE.26.024357

Publication date:
2018

Document Version
Publisher's PDF, also known as Version of record

Link back to DTU Orbit

Citation (APA):
Selim Habib, M. D., Markos, C., Enrique Antonio-Lopez, J., Correa, R. A., Bang, O., & Bache, M. (2018). Multi-stage generation of extreme ultraviolet dispersive waves by tapering gas-filled hollow-core anti-resonant fibers. *Optics Express*, *26*(19), 24357-24371. https://doi.org/10.1364/OE.26.024357

General rights
Copyright and moral rights for the publications made accessible in the public portal are retained by the authors and/or other copyright owners and it is a condition of accessing publications that users recognise and abide by the legal requirements associated with these rights.

- Users may download and print one copy of any publication from the public portal for the purpose of private study or research.
- You may not further distribute the material or use it for any profit-making activity or commercial gain
- You may freely distribute the URL identifying the publication in the public portal

If you believe that this document breaches copyright please contact us providing details, and we will remove access to the work immediately and investigate your claim.

Research Article | Vol. 26, No. 19 | 17 Sep 2018 | OPTICS EXPRESS 24357
Optics EXPRESS

Multi-stage generation of extreme ultraviolet dispersive waves by tapering gas-filled hollow-core anti-resonant fibers

MD. SELIM HABIB,[1,2,*] CHRISTOS MARKOS,[1] J. ENRIQUE ANTONIO-LOPEZ,[2] RODRIGO AMEZCUA CORREA,[2] OLE BANG,[1] AND MORTEN BACHE[1]

[1] *DTU Fotonik, Technical University of Denmark, Kgs. Lyngby, DK-2800, Denmark*
[2] *CREOL, The College of Optics and Photonics, University of Central Florida, Orlando, FL-32816, USA*
[*] *mdselim.habib@creol.ucf.edu*

Abstract: In this work, we numerically investigate an experimentally feasible design of a tapered Ne-filled hollow-core anti-resonant fiber and we report multi-stage generation of dispersive waves (DWs) in the range 90-120 nm, well into the extreme ultraviolet (UV) region. The simulations assume a 800 nm pump pulse with 30 fs 10 μJ pulse energy, launched into a 9 bar Ne-filled fiber with a 34 μm initial core diameter that is then tapered to a 10 μm core diameter. The simulations were performed using a new model that provides a realistic description of both loss and dispersion of the resonant and anti-resonant spectral bands of the fiber, and also importantly includes the material loss of silica in the UV. We show that by first generating solitons that emit DWs in the far-UV region in the pre-taper section, optimization of the following taper structure can allow re-collision with the solitons and further up-conversion of the far-UV DWs to the extreme-UV with energies up to 190 nJ in the 90-120 nm range. This process provides a new way to generate light in the extreme-UV spectral range using relatively low gas pressure.

© 2018 Optical Society of America under the terms of the OSA Open Access Publishing Agreement

OCIS codes: (060.5295) Photonic crystal fibers; (060.5530) Pulse propagation and temporal solitons; (190.7110) Ultrafast nonlinear optics; (190.7220) Upconversion.

References and links

1. T. Kobayashi and Y. Kida, "Ultrafast spectroscopy with sub-10 fs deep-ultraviolet pulses," Phys. Chem. Chem. Phys. **14**, 6200–6210 (2012).
2. N. Tamai and H. Miyasaka, "Ultrafast dynamics of photochromic systems," Chem. Rev. **100**, 1875–1890 (2000).
3. F. Reinert and S. Hüfner, "Photoemission spectroscopy - from early days to recent applications," New J. Phys. **7**, 97 (2005).
4. S. Hanna, P. Campuzano-Jost, E. Simpson, D. Robb, I. Burak, M. Blades, J. Hepburn, and A. Bertram, "A new broadly tunable (7.4-10.2ev) laser based VUV light source and its first application to aerosol mass spectrometry," Int. J. Mass Spectrom. **279**, 134 – 146 (2009).
5. M. C. Asplund, P. T. Snee, J. S. Yeston, M. J. Wilkens, C. K. Payne, H. Yang, K. T. Kotz, H. Frei, R. G. Bergman, and C. B. Harris, "Ultrafast UV pump/IR probe studies of C-H activation in linear, cyclic, and aryl hydrocarbons," J. Am. Chem. Soc. **124**, 10605–10612 (2002).
6. F. Yu and J. C. Knight, "Negative curvature hollow-core optical fiber," IEEE J. Sel. Top. Quantum Electron. **22**, 146–155 (2016).
7. C. Wei, R. J. Weiblen, C. R. Menyuk, and J. Hu, "Negative curvature fibers," Adv. Opt. Photon. **9**, 504–561 (2017).
8. C. Markos, J. C. Travers, A. Abdolvand, B. J. Eggleton, and O. Bang, "Hybrid photonic-crystal fiber," Rev. Mod. Phys. **89**, 045003 (2017).
9. A. D. Pryamikov, A. S. Biriukov, A. F. Kosolapov, V. G. Plotnichenko, S. L. Semjonov, and E. M. Dianov, "Demonstration of a waveguide regime for a silica hollow - core microstructured optical fiber with a negative curvature of the core boundary in the spectral region > 3.5 μm," Opt. Express **19**, 1441–1448 (2011).
10. A. N. Kolyadin, A. F. Kosolapov, A. D. Pryamikov, A. S. Biriukov, V. G. Plotnichenko, and E. M. Dianov, "Light transmission in negative curvature hollow core fiber in extremely high material loss region," Opt. Express **21**, 9514–9519 (2013).
11. F. Yu, W. J. Wadsworth, and J. C. Knight, "Low loss silica hollow core fibers for 3–4 μm spectral region," Opt. Express **20**, 11153–11158 (2012).

#337859 https://doi.org/10.1364/OE.26.024357
Journal © 2018 Received 4 Jul 2018; revised 20 Aug 2018; accepted 22 Aug 2018; published 4 Sep 2018

Optics EXPRESS

12. M. S. Habib, O. Bang, and M. Bache, "Low-loss hollow-core silica fibers with adjacent nested anti-resonant tubes," Opt. Express **23**, 17394–17406 (2015).
13. W. Belardi and J. C. Knight, "Hollow antiresonant fibers with reduced attenuation," Opt. Lett. **39**, 1853–1856 (2014).
14. W. Belardi and J. C. Knight, "Hollow antiresonant fibers with low bending loss," Opt. Express **22**, 10091–10096 (2014).
15. F. Poletti, "Nested antiresonant nodeless hollow core fiber," Opt. Express **22**, 23807–23828 (2014).
16. M. S. Habib, O. Bang, and M. Bache, "Low-loss single-mode hollow-core fiber with anisotropic anti-resonant elements," Opt. Express **24**, 8429–8436 (2016).
17. M. S. Habib, O. Bang, and M. Bache, "Low-loss hollow-core anti-resonant fibers with semi-circular nested tubes," IEEE J. Sel. Top. Quantum Electron. **22**, 156–161 (2016).
18. B. Debord, A. Amsanpally, M. Chafer, A. Baz, M. Maurel, J. M. Blondy, E. Hugonnot, F. Scol, L. Vincetti, F. Gérôme, and F. Benabid, "Ultralow transmission loss in inhibited-coupling guiding hollow fibers," Optica. **4**, 209–217 (2017).
19. F. Yu, M. Xu, and J. C. Knight, "Experimental study of low-loss single-mode performance in anti-resonant hollow-core fibers," Opt. Express **24**, 12969–12975 (2016).
20. R. M. Carter, F. Yu, W. J. Wadsworth, J. D. Shephard, T. Birks, J. C. Knight, and D. P. Hand, "Measurement of resonant bend loss in anti-resonant hollow core optical fiber," Opt. Express **25**, 20612–20621 (2017).
21. P. Uebel, M. C. Günendi, M. H. Frosz, G. Ahmed, N. N. Edavalath, J.-M. Ménard, and P. S. Russell, "Broadband robustly single-mode hollow-core pcf by resonant filtering of higher-order modes," Opt. Lett. **41**, 1961–1964 (2016).
22. N. Y. Joly, J. Nold, W. Chang, P. Hölzer, A. Nazarkin, G. K. L. Wong, F. Biancalana, and P. S. J. Russell, "Bright spatially coherent wavelength-tunable deep-UV laser source using an Ar-filled photonic crystal fiber," Phys. Rev. Lett. **106**, 203901 (2011).
23. G. Chang, L.-J. Chen, and F. X. Kärtner, "Fiber-optic cherenkov radiation in the few-cycle regime," Opt. Express **19**, 6635–6647 (2011).
24. K. F. Mak, J. C. Travers, P. Hölzer, N. Y. Joly, and P. S. J. Russell, "Tunable vacuum-UV to visible ultrafast pulse source based on gas-filled kagome-PCF," Opt. Express **21**, 10942–10953 (2013).
25. F. Belli, A. Abdolvand, W. Chang, J. C. Travers, and P. S. Russell, "Vacuum-ultraviolet to infrared supercontinuum in hydrogen-filled photonic crystal fiber," Optica **2**, 292–300 (2015).
26. A. Ermolov, K. F. Mak, M. H. Frosz, J. C. Travers, and P. S. J. Russell, "Supercontinuum generation in the vacuum ultraviolet through dispersive-wave and soliton-plasma interaction in a noble-gas-filled hollow-core photonic crystal fiber," Phys. Rev. A **92**, 033821 (2015).
27. F. Köttig, F. Tani, J. C. Travers, and P. S. J. Russell, "PHz-wide spectral interference through coherent plasma-induced fission of higher-order solitons," Phys. Rev. Lett. **118**, 263902 (2017).
28. F. Köttig, D. Novoa, F. Tani, M. C. Günendi, M. Cassataro, J. C. Travers, and P. S. Russell, "Mid-infrared dispersive wave generation in gas-filled photonic crystal fibre by transient ionization-driven changes in dispersion," Nat. Com. **8**, 813– (2017).
29. M. Michieletto, J. K. Lyngsø, C. Jakobsen, J. Lægsgaard, O. Bang, and T. T. Alkeskjold, "Hollow-core fibers for high power pulse delivery," Opt. Express **24**, 7103–7119 (2016).
30. A. Urich, R. R. J. Maier, F. Yu, J. C. Knight, D. P. Hand, and J. D. Shephard, "Flexible delivery of Er:YAG radiation at 2.94 μm with negative curvature silica glass fibers: a new solution for minimally invasive surgical procedures," Biomed. Opt. Express **4**, 193–205 (2013).
31. P. Jaworski, F. Yu, R. R. Maier, W. J. Wadsworth, J. C. Knight, J. D. Shephard, and D. P. Hand, "Picosecond and nanosecond pulse delivery through a hollow-core negative curvature fiber for micro-machining applications," Opt. Express **21**, 22742–22753 (2013).
32. J. C. Travers, W. Chang, J. Nold, N. Y. Joly, and P. S. J. Russell, "Ultrafast nonlinear optics in gas-filled hollow-core photonic crystal fibers (invited)," J. Opt. Soc. Am. B **28**, A11–A26 (2011).
33. P. S. J. Russell, P. Hölzer, W. Chang, A. Abdolvand, and J. C. Travers, "Hollow-core photonic crystal fibres for gas-based nonlinear optics," Nat. Photon. **8**, 278–286 (2014).
34. P. Hölzer, W. Chang, J. C. Travers, A. Nazarkin, J. Nold, N. Y. Joly, M. F. Saleh, F. Biancalana, and P. S. J. Russell, "Femtosecond nonlinear fiber optics in the ionization regime," Phys. Rev. Lett. **107**, 203901 (2011).
35. M. F. Saleh and F. Biancalana, "Understanding the dynamics of photoionization-induced nonlinear effects and solitons in gas-filled hollow-core photonic crystal fibers," Phys. Rev. A **84**, 063838 (2011).
36. M. F. Saleh, W. Chang, J. C. Travers, P. S. J. Russell, and F. Biancalana, "Plasma-induced asymmetric self-phase modulation and modulational instability in gas-filled hollow-core photonic crystal fibers," Phys. Rev. Lett. **109**, 113902 (2012).
37. M. S. Habib, C. Markos, O. Bang, and M. Bache, "Soliton-plasma nonlinear dynamics in mid-IR gas-filled hollow-core fibers," Opt. Lett. **42**, 2232–2235 (2017).
38. D. Novoa, M. Cassataro, J. C. Travers, and P. S. J. Russell, "Photoionization-induced emission of tunable few-cycle midinfrared dispersive waves in gas-filled hollow-core photonic crystal fibers," Phys. Rev. Lett. **115**, 033901 (2015).
39. S.-J. Im, A. Husakou, and J. Herrmann, "High-power soliton-induced supercontinuum generation and tunable sub-10-fs VUV pulses from kagome-lattice HC-PCFs," Opt. Express **18**, 5367–5374 (2010).
40. W. Chang, A. Nazarkin, J. C. Travers, J. Nold, P. Hölzer, N. Y. Joly, and P. S. Russell, "Influence of ionization on ultrafast gas-based nonlinear fiber optics," Opt. Express **19**, 21018–21027 (2011).
41. F. Köttig, F. Tani, C. M. Biersach, J. C. Travers, and P. S. Russell, "Generation of microjoule pulses in the deep

Optics EXPRESS

ultraviolet at megahertz repetition rates," Optica **4**, 1272–1276 (2017).
42. S. P. Stark, J. C. Travers, and P. S. J. Russell, "Extreme supercontinuum generation to the deep UV," Opt. Lett. **37**, 770–772 (2012).
43. S. Sørensen, U. Møller, C. Larsen, P. Moselund, C. Jakobsen, J. Johansen, T. Andersen, C. Thomsen, and O. Bang, "Deep-blue supercontinnum sources with optimum taper profiles - verification of GAM," Opt. Express **20**, 10635–10645 (2012).
44. M. Bache, M. S. Habib, C. Markos, and J. Lægsgaard, "Poor-man's model of hollow-core anti-resonant fibers," arXiv:180610416 (2018).
45. F. Tani, F. Köttig, D. Novoa, R. Keding, and P. S. Russell, "Effect of anti-crossings with cladding resonances on ultrafast nonlinear dynamics in gas-filled photonic crystal fibers," Photon. Res. **6**, 84–88 (2018).
46. R. Sollapur, D. Kartashov, M. Zürch, A. Hoffmann, T. Grigorova, G. Sauer, A. Hartung, A. Schwuchow, J. Bierlich, J. Kobelke, M. Chemnitz, M. A. Schmidt, and C. Spielmann, "Resonance-enhanced multi-octave supercontinuum generation in antiresonant hollow-core fibers," Light. Sci. &Amp; Appl. **6**, e17124– (2017).
47. R. Kitamura, L. Pilon, and M. Jonasz, "Optical constants of silica glass from extreme ultraviolet to far infrared at near room temperature," Appl. Opt. **46**, 8118–8133 (2007).
48. G. L. Tan, M. F. Lemon, D. J. Jones, and R. H. French, "Optical properties and london dispersion interaction of amorphous and crystalline SiO_2 determined by vacuum ultraviolet spectroscopy and spectroscopic ellipsometry," Phys. Rev. B **72**, 205117 (2005).
49. G. Ghosh, M. Endo, and T. Iwasaki, "Temperature-dependent sellmeier coefficients and chromatic dispersions for some optical fiber glasses," J. Light. Techn. **12**, 1338 –1342 (1994).
50. C. R. Petersen, R. D. Engelsholm, C. Markos, L. Brilland, C. Caillaud, J. Trolès, and O. Bang, "Increased mid-infrared supercontinuum bandwidth and average power by tapering large-mode-area chalcogenide photonic crystal fibers," Opt. Express **25**, 15336–15348 (2017).
51. M. Miyagi and S. Kawakami, "Design theory of dielectric-coated circular metallic waveguides for infrared transmission," J. Light. Technol. **2**, 116–126 (1984).
52. J. L. Archambault, R. J. Black, S. Lacroix, and J. Bures, "Loss calculations for antiresonant waveguides," J. Light. Technol. **11**, 416–423 (1993).
53. M. Zeisberger and M. A. Schmidt, "Analytic model for the complex effective index of the leaky modes of tube-type anti-resonant hollow core fibers," Sci. Reports **7**, 11761 (2017).
54. E. A. J. Marcatili and R. A. Schmeltzer, "Hollow metallic and dielectric waveguides for long distance optical transmission and lasers," Bell Syst. Tech. J. **43**, 1783–1809 (1964).
55. M. F. Saleh, W. Chang, P. Hölzer, A. Nazarkin, J. C. Travers, N. Y. Joly, P. S. J. Russell, and F. Biancalana, "Theory of photoionization-induced blueshift of ultrashort solitons in gas-filled hollow-core photonic crystal fibers," Phys. Rev. Lett. **107**, 203902 (2011).
56. A. B. Fedotov, E. E. Serebryannikov, and A. M. Zheltikov, "Ionization-induced blueshift of high-peak-power guided-wave ultrashort laser pulses in hollow-core photonic-crystal fibers," Phys. Rev. A **76**, 053811 (2007).
57. M. A. Finger, N. Y. Joly, T. Weiss, and P. S. Russell, "Accuracy of the capillary approximation for gas-filled kagome-style photonic crystal fibers," Opt. Lett. **39**, 821–824 (2014).
58. A. Börzsönyi, Z. Heiner, M. P. Kalashnikov, A. P. Kovács, and K. Osvay, "Dispersion measurement of inert gases and gas mixtures at 800 nm," Appl. Opt. **47**, 4856–4863 (2008).
59. A. Börzsönyi, Z. Heiner, A. Kovács, M. P. Kalashnikov, and K. Osvay, "Measurement of pressure dependent nonlinear refractive index of inert gases," Opt. Express **18**, 25847–25854 (2010).
60. A. Couairon and A. Mysyrowicz, "Femtosecond filamentation in transparent media," Phys. Rep. **441**, 47–189 (2007).

1. Introduction

The vacuum UV (VUV) spectral range (10-200 nm) is of great technical and scientific interest because it is associated with an extensive range of applications, such as transient absorption spectroscopy [1], ultrafast photochromic dynamics [2], photoemission spectroscopy [3], photoionization mass spectroscopy [4], and control of chemical reactions [5]. However, the availability of femtosecond laser sources in that spectral region is scarce: standard frequency conversion of near-IR lasers in crystals is limited to the near-UV (NUV, 300-400 nm) and mid-UV (MUV, 200-300 nm), while in the far-UV (FUV, 120-200 nm) and extreme-UV (XUV, 10-120 nm) the UV losses and lack of phase-matching conditions make harmonic conversion in crystals difficult or even impossible. In turn, harmonic generation in gas jets require high-energy pulses from low-repetition rate lasers and has low yield.

Hollow-core anti-resonant (HC-AR) fibers [6–8] are currently revolutionizing the fiber optics community. By structurally optimizing the cladding tubes surrounding the fiber core (shape, size, position, number), extremely low propagation loss can be achieved, the bend loss can be

Optics EXPRESS

reduced, the fiber can be effectively made single-mode, and can have 40+ dB extinction ratio between the field in the gas-filled core and the field in the glass cladding [9–21]. Especially the latter allows using the well-established telecommunication silica fiber production platform to achieve low-loss, broadband guidance in the important UV and mid-IR ranges [9–12, 22–28], and high-power delivery of pulsed lasers [29–31]. Compared to propagation in bulk, gas-filled HC-AR fibers also has remarkable properties for ultrafast nonlinear optics, such as extremely high damage threshold, tunable dispersion and nonlinearity through the gas pressure, and very long confinement lengths [32, 33]. Finally, at high intensities ionization of the gas results in plasma formation [34], which because it is confined in a fiber is promising to spark a new era of filament-based nonlinear optics [26, 27, 35–38].

Recent work has focused on using HC-AR fibers to solve the challenge of providing access to energetic ultrashort UV laser sources [22, 24–28, 39, 40]. Bright emission of mid-UV pulses using Ar-filled HC fiber was first predicted [39] and later experimentally confirmed in [22]. This relied on efficient generation of UV dispersive waves (DWs) by the well-known process of soliton self-compression to the sub single-cycle regime, followed by resonant DW radiation. Later work [25–28, 41] used the same approach to study further how to go deeper into the UV and achieving higher power. UV light generation at 280 nm was also reported in a solid-core photonic crystal fiber (PCF) by employing a sharp tapering section [42], however, the generation of VUV light was limited due to the strong material absorption in the VUV range. Conventional long-pulse SCG in solid-core PCFs the UV edge is also given by DWs, but here the edge is limited to the wavelength that is group-velocity matched to the shortest of either the loss edge or the 2. zero-dispersion wavelength [43].

To date the work on VUV light generation in gas-filled HC-AR fibers has been carried out in uniform HC-AR fibers. Achieving phase-matching deep into the UV is facilitated by light gases like He or Ne (being less dispersive and having a higher ionization potential leading to reduced plasma losses [41]), small-core fibers and low pressures [26]. However, decreasing the core size increases the propagation loss, and low-pressure light gases have a significantly reduced nonlinearity.

In this work we numerically demonstrate (for the first time to the best of our knowledge) how to alleviate some of these issues by using a tapered Ne-filled HC-AR fiber. This fiber is used with a light noble gas under medium pressure, and in the first stage where the core is large soliton self-compression leads to generation of multiple DWs in the far-UV region. These are then in the tapering section converted to XUV DWs through re-collision with the parent solitons. Due to the decreasing core size in the taper the process is shown to reach record-low XUV wavelengths, even below 100 nm. The taper helps keeping propagation losses at a minimum because the interaction in the high-loss small-core section is very limited in length. We show how every section of the taper profile (transition length, waist, up-taper) has a crucial role in the soliton-plasma dynamics, which eventually directly affects the location and intensity of the generated DWs. In other words the taper profile should be carefully designed. In order to provide accurate numerical simulations of the continuous transitions of the fiber loss and dispersion resonances throughout the taper section, we had to develop a new analytical model [44]. It is able to extend the simple capillary model to include loss and dispersion resonances without any significant assumptions.

2. Dispersion and loss of HC-AR fiber taper

We seek to accurately model the XUV to near-IR nonlinear behavior of gas-filled HC-AR fibers. This is already a substantially complex task in a straight fiber due to the presence of a number of anti-resonant and resonant spectral regions, affecting both losses and dispersion across the wavelength range. An additional challenge in our case is that in the tapering section the fiber is scaled down in critical parameters (core size, thickness of cladding AR elements). Currently the accepted approach to model these fibers is to use the the so-called Marcatili-Schmeltzer (MS)

Optics EXPRESS

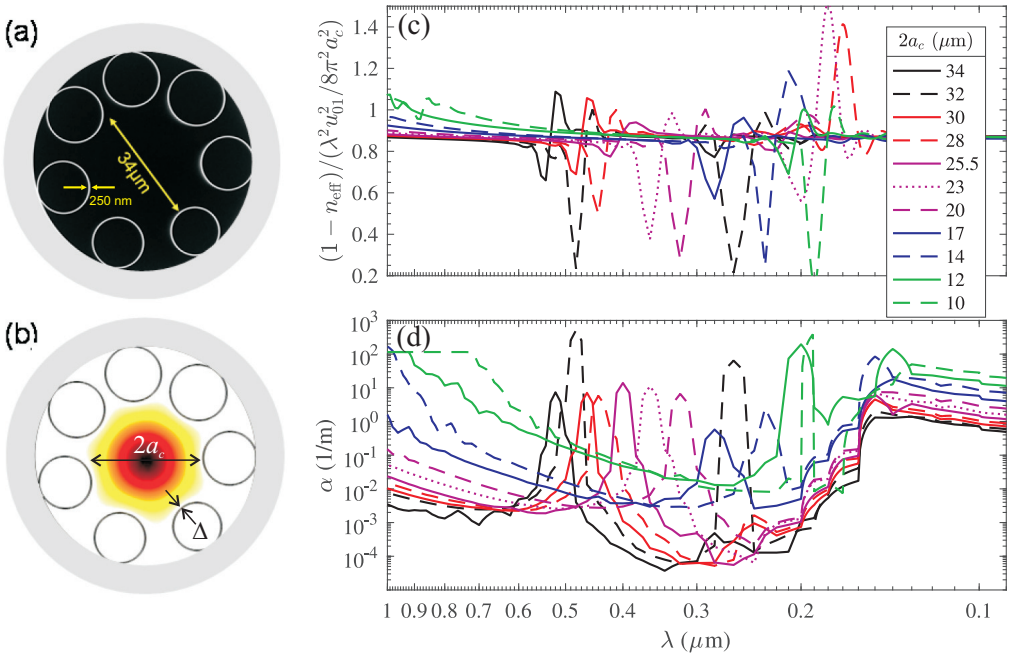

Fig. 1. (a) SEM image of a fabricated HC-AR silica fiber with 7 AR cladding tubes, 250 nm tube-wall thickness and 34 μm core diameter. (b) The FEM design used in this paper is based on the fiber (a), and the FEM structure is shown overlapped with the fundamental mode at 800 nm. (c) and (d) FEM data of calculated effective index for an evacuated fiber and loss vs. wavelength. The effective index is scaled to the vacuum MS dispersion, see text for details. The original fiber ($2a_c$ = 34 μm and Δ = 250 nm) was used as a starting point, and the shown cores sizes are then considered linearly tapered so Δ is scaled accordingly down.

capillary model in the nonlinear Schrödinger-like equation (NLSE) and neglect the resonances and how they affect the dispersion and loss. Only recently was dispersion and loss data from a full finite-element model (FEM) used directly in NLSE modeling of pulse propagation in an HC-AR fiber [37], while other approaches employed a Lorentzian extension of the MS model [45,46]. It is clear that accurate modeling of the resonances and the losses of these fibers is crucial, especially for predicting the UV behavior where the glass in the cladding becomes very lossy.

A scanning electron microscope (SEM) image of the HC-AR fiber used in our calculations is shown in Fig. 1(a). The HC-AR fiber has a core diameter of $2a_c$ = 34 μm, an average capillary diameter of 16 μm, and an average silica wall thickness of Δ = 250 nm. The wall thickness was chosen to give a first AR transmission band centered at 800 nm. Figure 1(b) shows the near-field profile of the fundamental mode of the imported cross-section structure, calculated using FEM.

It is important to mention that careful consideration of the silica refractive index is required for wavelengths less than 210 nm due to the absorption by impurities and the presence of OH groups and point defects [47,48]. In turn, the standard Sellmeier equation holds well in the range $\lambda > 0.210$ μm [44,47]. Therefore, we used the standard Sellmeier equation [49] for $\lambda > 0.210$ μm and the measured refractive index data of silica for $\lambda < 0.210$ μm (suitably interpolated to the chosen COMSOL data points) to calculate the mode propagation constant β and confinement loss α using the FEM-based COMSOL software. Importantly, we allowed the refractive index of silica to be complex in the FEM calculations, in order to account for the material losses in the UV. This approach is different than our previous work where the silica loss was not considered in the FEM calculation and the material-based loss was added afterwards based on the power-fraction

Optics EXPRESS

of light in silica [12]. To get an accurate calculation of the loss, we used a perfectly-matched layer outside the fiber domain and great care was taken to optimize both mesh size and the parameters of the perfectly-matched layer [12, 15, 17].

Figure 2(a) shows the taper profile of the fiber used in our work with the optimum values of the length of the uniform waist section (L_W), the down-taper section (L_T), and the uniform input or before taper section (L_{BT}). The core diameter of the L_{BT} and L_W sections was 34 μm and 10 μm, respectively. The former is a quite typical value for 800 nm pumping, and can easily handle 10's of μJ of pump energy. The latter waist value was chosen to give access to dispersive wave phase-matching deep into the XUV.

In our model, we assume a linear decrease in silica wall thickness during the taper transition from 34 to 10 μm as just as the hole-to-hole pitch to a good approximation has been found to decrease linearly in tapered solid-core PCFs [50]. The silica wall thickness of L_{BT} is initially 250 nm, which then decreases linearly to 74 nm in the taper waist section. This dramatically affects the resonance wavelengths, and thus both dispersion and loss of the fiber modes. We carefully modeled 11 different core sizes from 10 to 34 μm and observed how the resonances changed. The aim was to be able to track the resonances in a gap-free manner as they change through the taper due to a reduced core diameter and wall thickness of the cladding tubes. The result is shown in Figs. 1(c) and (d). Here we clearly see how the loss resonances in (d) shift from the visible towards the UV as the fiber is tapered down, and at the resonance peaks there are associated dispersion resoances in the effective mode index, (c). The effective index scaling we use in Fig. 1(c) is chosen from Eq. (1) that we derive later, which shows that in the vacuum case the celebrated MS capillary model gives $n_{\mathrm{eff,MS}} \simeq 1 - u_{mn}^2/(2a_c^2k_0^2)$. Thus, the scaled effective mode index of the fundamental hybrid mode is then unity when the scaling is chosen as $(1 - n_{\mathrm{eff,MS}})/[u_{01}^2/(2a_c^2k_0^2)]$, where $u_{01} \simeq 2.405$ is the first zero of the 0'th order Bessel function of the first kind, and $k_0 = \omega_0/c = 2\pi/\lambda_0$ is the vacuum wavenumber.

However, implementing these data sets in the NLSE it turned out that much more than 11 FEM data sets are needed to do this since the resonance wavelengths significantly change from one core size to the next; this made it almost impossible to do a smooth interpolation during the tapering section. We therefore decided to investigate various strategies for a more analytical approach that could allow us to calculate the resonances for any core size and cladding tube wall thickness [44]. We developed a so-called poor-man's model as an analytical extension of the celebrated MS capillary model. It can accurately describe the full dispersion and loss profiles of AR-HC fibers, covering all resonance and anti-resonance regions in a gap-free manner. Being analytical in nature it works for any core size, cladding wall thickness and glass-cladding material. All the model needs is a single quite general fitting parameter to match the overall loss level to a single FEM simulation, which serves as a standard for the chosen HC-AR fiber design (e.g. circular or elliptical cladding tubes, nested or no nested cladding tubes etc.). We refer to [44] for more details, but briefly we start with the MS model and calculate the core modes of an evacuated capillary having a core radius a_c and a capillary thickness Δ. The core modes are Bessel functions of the first kind $\propto J_m(\kappa r)$. Here we have introduced the core transverse wavenumber $\kappa = k_0\sqrt{1 - n_{\mathrm{eff,MS}}^2}$ Here $n_{\mathrm{eff,MS}}$ is the effective index of the mode, as calculated from the eigenvalue problem, and in the specific case of an evacuated fiber under the perfect-conductor assumption, yielding $\kappa a_c = u_{mn}$, we have the simple relation

$$n_{\mathrm{eff,MS}} = \sqrt{1 - \frac{u_{mn}^2}{a_c^2k_0^2}} \simeq 1 - \frac{u_{mn}^2}{2a_c^2k_0^2} \tag{1}$$

where u_{mn} is the n'th zero of the m'th order Bessel function J_m. In the dielectric the transverse wavenumber is $\sigma = k_0\sqrt{n_d^2 - n_{\mathrm{eff,MS}}^2}$where n_d is the dielectric refractive index. Since for a hollow fiber $n_{\mathrm{eff,MS}} \simeq 1$, irrespective of whether the fiber is evacuated or gas-filled, we can to a good

Optics EXPRESS

approximation write $\sigma \simeq k_0\sqrt{n_d^2 - 1}$. We may analytically calculate the mode loss in this thin capillary. This is done with a bouncing-ray (BR) model, and the loss coefficients for the TE and TM modes are then [44]

$$\alpha_{\mathrm{TE,BR}} = \frac{2u_{mn}}{a_c^2 k_0[4\cos^2(\sigma\Delta) + (\frac{\sigma}{\kappa} + \frac{\kappa}{\sigma})^2 \sin^2(\sigma\Delta)]} \tag{2}$$

$$\alpha_{\mathrm{TM,BR}} = \frac{2u_{mn}}{a_c^2 k_0[4\cos^2(\sigma\Delta) + (\frac{\sigma}{n_d^2\kappa} + \frac{n_d^2\kappa}{\sigma})^2 \sin^2(\sigma\Delta)]} \tag{3}$$

For hybrid modes, including the fundamental mode found by setting $m = 0$ and taking the first zero $n = 1$, the loss is taken as a geometric average.

$$\alpha_{\mathrm{H,BR}} = (\alpha_{\mathrm{TE,BR}} + \alpha_{\mathrm{TM,BR}})/2 \tag{4}$$

We remark that this is as far as we know the first analytical direct calculation of the HC-AR fiber loss without resorting to perturbative methods. As we discuss in detail in [44] alternative, perturbative methods [51–53] do not give correct values at the resonance loss peaks.

Next we use a perturbative approach to calculate the associated dispersion. Such a pertubative method for calculating the loss and dispersion was already shown in the original MS model for an infinitely thick capillary [54]. It turns out that the perturbative expressions in [54] can be generalized to hold also for a thin capillary if we take the capillary material impedance and admittance and replace it with the impedance and admittance of a thin capillary surrounded by vacuum [44]. This gives the following expressions for the effective index and power loss coefficient for a hybrid mode

$$n_{\mathrm{eff,p}} = n_{\mathrm{eff,MS}} - \frac{u_{mn}^2}{a_c^3 k_0^3}\mathrm{Im}(Z_{\mathrm{H}}) \tag{5}$$

$$\alpha_{\mathrm{H,p}} = \frac{2u_{mn}^2}{a_c^3 k_0^2}\mathrm{Re}(Z_{\mathrm{H}}) \tag{6}$$

where $Z_{\mathrm{H}} = (Z_{\mathrm{TE}} + Y_{\mathrm{TM}})/2$ is the hybrid mode impedance, calculated as an average of the TE impedance and the TM admittance. The critical next step is to get an accurate expression of the impedance. We found [44] that the analytical impedance expressions (also found in, e.g., [51,52]) yield a too high loss at the AR resonances compared to the BR model we derived above. The inaccuracy of the loss at the peaks was also acknowledged in [51,52], and it basically occurs because the perturbative approach breaks down exactly around the resonances. In contrast, the BR model has no restrictions, and Eq. (4) must hold. Therefore to get the perturbative loss to match that of the BR model, $\alpha_{\mathrm{H,BR}} = \alpha_{\mathrm{H,p}}$, we suggested using the following modified impedances [44]

$$\hat{Z}_{\mathrm{TE}} = Z_0 \frac{\frac{1}{2} - i(\frac{\sigma}{\kappa} + \frac{\kappa}{\sigma})^{-1}\tan(\sigma\Delta)}{2 - i(\frac{\sigma}{\kappa} + \frac{\kappa}{\sigma})\tan(\sigma\Delta)} \tag{7}$$

$$\hat{Y}_{\mathrm{TM}} = Y_0 \frac{\frac{1}{2} - i(\frac{\sigma}{n_d^2\kappa} + \frac{n_d^2\kappa}{\sigma})^{-1}\tan(\sigma\Delta)}{2 - i(\frac{\sigma}{n_d^2\kappa} + \frac{n_d^2\kappa}{\sigma})\tan(\sigma\Delta)} \tag{8}$$

where $Z_0 = k_0/\kappa$, $Y_0 = n_0^2 Z_0 = Z_0$ (where $n_0 = 1$ is the core refractive index) and the hat denotes that the equations have been empirically modified to match the loss of the BR model.

Finally, in [44] we also showed how the mode losses can be calculated using this model if the dielectric is lossy $\bar{n}_d = n_d + i\tilde{n}_d$. Based on work by [52], we found that we must replace the

Optics EXPRESS

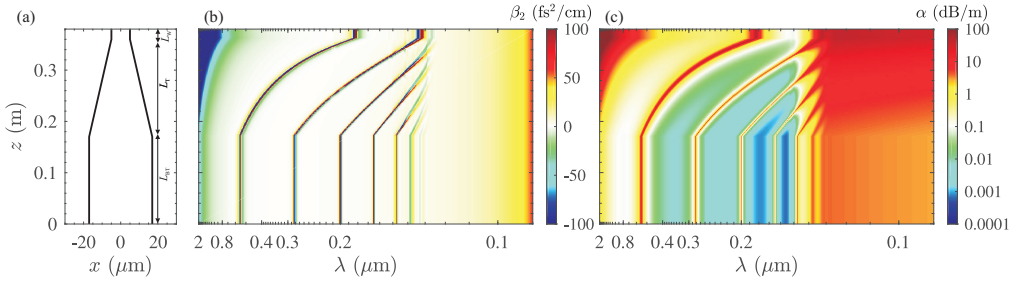

Fig. 2. (a) Basic fiber taper layout with $L_{\mathrm{BT}} = 17$ cm of untapered fiber with 34 μm core diameter followed by $L_{\mathrm{T}} = 19$ cm taper to a 10 μm core size and $L_{\mathrm{W}} = 2$ cm waist after the taper. For a fiber filled with 9 bar Ne, (b) and (c) show the hybrid fundamental mode's GVD and loss vs. wavelength (log scale) using the poor-man's model [44], i.e. using Eqs. (5)-(11).

transverse wavenumber ratio σ/κ for the TE case with

$$\left(\frac{\sigma}{\kappa}\right)^* = \frac{\sigma}{\kappa}\frac{1+\frac{\kappa}{\sigma}\tanh(n_d\tilde{n}_d Z_d^2\sigma\Delta)}{1+\frac{\sigma}{\kappa}\tanh(n_d\tilde{n}_d Z_d^2\sigma\Delta)} \tag{9}$$

where $Z_d = (n_d^2-1)^{-1/2}$. Similarly for the TM case we must replace $\sigma/(n_d^2\kappa)$ with

$$\left(\frac{\sigma}{n_d^2\kappa}\right)^* = \frac{\sigma}{n_d^2\kappa}\frac{1+\frac{n_d^2\kappa}{\sigma}\tanh(n_d\tilde{n}_d Z_d^2\sigma\Delta)}{1+\frac{\sigma}{n_d^2\kappa}\tanh(n_d\tilde{n}_d Z_d^2\sigma\Delta)} \tag{10}$$

With these extensions we can evaluate analytically the expected mode loss due to the UV material loss in silica. In addition, the model directly gives the associated dispersion resonances through Eq. (5).

To complete the poor-man's model for the losses we include an overall adjustment factor f_{FEM} that allows us to adjust the calculated spectral loss shape to match the levels found in the FEM data, so the total loss is

$$\alpha_{\mathrm{PMM}} = f_{\mathrm{FEM}}\alpha_{\mathrm{capillary}} \tag{11}$$

where $\alpha_{\mathrm{capillary}}$ is the calculated capillary loss of the mode, i.e. either TE, TM or hybrid. We found that $f_{\mathrm{FEM}} = 10^{-2}$ gave good agreement with the FEM data of the fundamental hybrid mode at various core sizes of the fiber shown in Fig. 1(a). This choice was a compromise between matching the loss in the anti-resonant regions and the UV loss plateau [44].

Having this semi-analytical model of the resonant and anti-resonant behavior of the HC-AR fiber, consisting of Eqs. (5)-(11), we can now get a complete picture of how the fiber properties change during the tapering section. Figs. 2(b) and (c) show the dramatic changes in the numerous resonances along the fiber taper section: the first resonance moves from 550 nm to 180 nm and the second resonance from 280 nm to 135 nm. The model captures all resonances, and an important point is that in the UV the resonances eventually disappear. This is because we include the imaginary part of the refractive index into the model. We used the measured refractive index data of silica from [47] to evaluate the complex refractive index for wavelengths from the XUV to the mid-IR. In the absence of material losses, when the core is large ($a_c k_0 \gg 1$) we have $\sigma/\kappa \gg 1$, which gives the characteristic dramatic changes from resonant to anti-resonant losses as the wavelength is changed; basically in this limit the $\sin^2(\sigma\Delta)$ is cyclically zero (resonance) or very large (anti-resonance) compared to the competing $\cos^2(\sigma\Delta)$ term in the denominator of the losses Eqs. (2)-(3). Instead when $\tilde{n}_d$ becomes significant, it turns out that $(\sigma/\kappa)^* \to 1$ (TE case)

Optics EXPRESS

and $(\sigma/n_d^2\kappa)^* \to 1$ (TM case). This implies that the modified impedances become constant and thus no resonances appear in the loss and dispersion. Specifically, in the loss equations in the denominators the $\cos^2(\sigma\Delta)$ and $\sin^2(\sigma\Delta)$ term now have the same prefactors, so they add up to unity, thus canceling the resonant/anti-resonant behavior. Some interesting observations can be made: the XUV loss is rather constant during the taper, which is mainly because material loss dominates the mode losses. It does increase to a critical level at the taper waist, > 10 dB/m. It is also worth noticing that the pump wavelength experiences very high losses at the end of the taper since it is now at the IR edge of the first anti-resonance band. Therefore the tapered fiber is not suitable for long propagation of neither the generated solitons nor the generated UV light.

3. Nonlinear pulse propagation model

The nonlinear optical pulse propagation was studied using a generalized nonlinear Schrödinger equation which also accounts free-electron effects described as [32, 55, 56]:

$$\left(i\partial_z + \hat{D}(i\partial_t) + i\frac{\alpha_{\mathrm{PMM}}}{2} + \gamma(1 + i\omega_0^{-1}\partial_t)|A|^2 - \frac{\omega_p^2(z,t)}{2\omega_0 c} + i\frac{A_{\mathrm{eff}} I_p \partial_t N_e}{2|A|^2}\right)A = 0 \tag{12}$$

where A is the complex field envelope centered around the central angular frequency ω_0, t is the time in the reference frame moving with the pump group velocity, $\hat{D}(i\partial_t) = \sum_{m\geq 2}\beta_m(i\partial_t)^m/m!$ is the full dispersion operator in time domain and β_m is the m^{th} order dispersion coefficient. The linear propagation constant of the gas-filled fiber was calculated using the following expression:

$$\beta(\lambda, p, T) = \frac{2\pi}{\lambda}\sqrt{n_{\mathrm{eff,p}}^2(\lambda) + \delta(\lambda)\frac{\rho(p,T)}{\rho_0}} \tag{13}$$

where $n_{\mathrm{eff,p}}(\lambda)$ is the effective mode index in an evacuated fiber, as calculated with the poor-man's model, and as described in [44] we use the UV and IR corrections to the MS dispersion in Eq. (5) by adopting a wavelength-dependent "area-preserving" core radius [57] with the parameters $s = 0.02$ and $a_{c,\mathrm{AP}} = 1.075a_c$. In addition, $\delta(\lambda)$ is the Sellmeier terms describing the gas deviation from vacuum [58], ρ_0 is the density of the material at standard temperature and pressure, and ρ is the density at pressure p and temperature T. The linear propagation loss of the fiber α_{PMM} does not depend on pressure, and was calculated using the poor-man's model.

As usual $\gamma = \omega_0 n_2/(cA_{\mathrm{eff}})$ is the fiber Kerr nonlinearity, where c is the velocity of light in vacuum, A_{eff} is the effective mode area of the fiber at the pump wavelength, and n_2 is the Kerr nonlinear coefficient of the gas, which scales linearly with pressure [59]. Self-steepening is included through the term $(1 + i\omega_0^{-1}\partial_t)$. Furthermore, $\omega_p(z,t) = e\sqrt{N_e(z,t)/\varepsilon_0 m_e}$ is the plasma frequency, m_e is the electron mass, ε_0 is the free space permittivity, I_p is the ionization energy of the gas, and $N_e(z,t)$ is the free electron density.

We neglect the Raman contribution of silica due to the very low light-glass overlap ($\ll 0.1\%$) [40]. The dynamics of ionization depends on the multiphoton or tunneling process which is determined by the Keldysh parameter [35, 55]. In this work, the peak intensity at the maximum compression point reaches 350 TW/cm^2 and tunneling ionization dominates over multiphoton ionization. The free electron density was calculated using quasi-static tunneling ionization based on the Ammosov, Delone, and Krainov model [35, 40]. The free electron density was calculated with [40] $N_e(t) = N_0\left(1 - \exp\left[-\int_{-\infty}^{t} W(t')dt'\right]\right)$ where $W(t)$ is the ionization rate, which was also calculated according to [40].

4. Numerical results

In the simulations we model an 800 nm 30 fs FWHM pulse with 10 μJ energy and 1 kHz repetition rate. The fiber is filled with 9 bar Ne; the pressure was chosen as a compromise between getting a

Optics EXPRESS

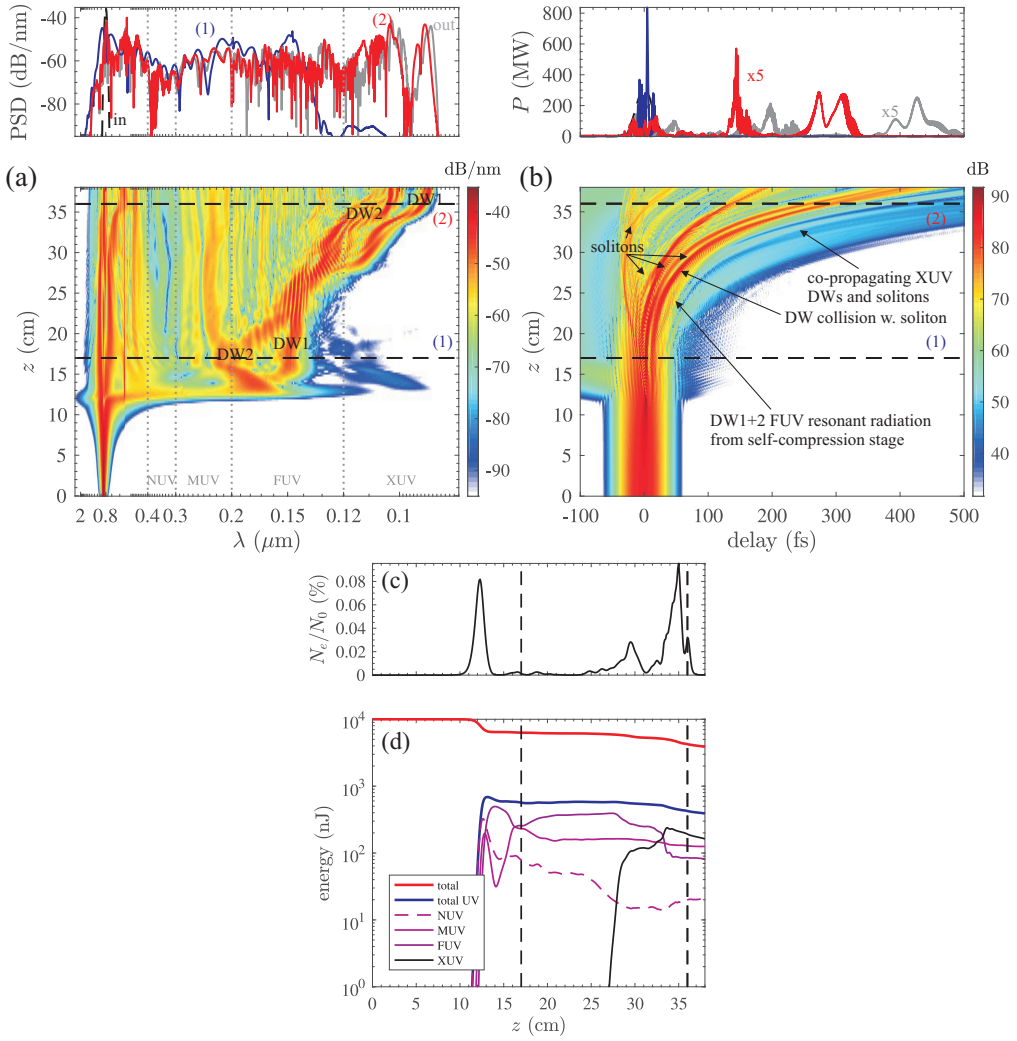

Fig. 3. Simulation of fiber taper shown in Fig. 2 using a 800 nm 30 fs 10 μJ input pulse. (a) Spectral evolution, shown as the power-spectral density (PSD) on a dB scale. Here the NUV, MUV, FUV and XUV sections are indicated with dotted lines, and the start (1) and finish (2) of the tapering section are indicated with dashed lines, and their snapshots are plotted with blue and red colors in the top plot. (b) Time evolution, shown with a dB scale to emphasize the DW dynamic; the snapshots at the end of the tapering section and fiber exit are amplified by a factor of 5 for better visualization. (c) Ionization fraction and (d) energy content in the various relevant sections of the spectrum vs. propagation distance.

high enough nonlinearity to get soliton pulse compression after around 10 cm with a reasonable pulse energy, yet still low enough to push the DW phase-matching points deep into the UV. The soliton order was $N = 5.1$.

Figure 3 shows a typical simulation where the untapered section is long enough for a soliton self-compression stage to form, which happens after 12 cm. This initial stage therefore gives us an indication of what kind of dynamics we would observe in a standard untapered fiber. At the self-compression stage, a sub-1 fs self-compressed soliton forms stretching from the near-IR to the FUV. In this process a strong FUV dispersive wave with 0.6 μJ total energy is generated at 170 nm.

Optics EXPRESS

This wavelength is consistent with phase-matching calculations of degenerate four-wave mixing between the self-compressed soliton and the DW [38]: $\beta_{\rm sol}(\omega_{\rm RR}) = \beta(\omega_{\rm RR})$, where $\omega_{\rm RR}$ is the resonant radiation frequency of the DW. Here $\beta_{\rm sol}(\omega) = \beta(\omega_0)+(\omega-\omega_0)\beta_1+\gamma P_{\rm sol}\omega/\omega_{\rm sol}-\frac{N_e}{2N_c}\frac{\omega_{\rm sol}^2}{c\omega}$ is the soliton dispersion relation including the Kerr nonlinear phase shift $\gamma P_{\rm sol}\omega/\omega_{\rm sol}$, where $P_{\rm sol}$ is the soliton peak power and $\omega/\omega_{\rm sol}$ accounts for self-steepening, and $-\frac{N_e}{2N_c}\frac{\omega_{\rm sol}^2}{c\omega}$ is the self-defocusing nonlinear plasma phase shift, where $N_c = \varepsilon_0 m_e\omega_0^2/e^2$ is the critical plasma density where it becomes opaque [60]. As the self-compressed soliton forms, it ionizes the gas partially, and this leads to a significant loss in the total energy. This ionization event is accompanied by soliton fission and it blue-shifts one of the solitons to below 500 nm, as we also will see later in the spectrograms in Fig. 4, and this actually red-shifts the first DW (175 nm) compared to what we would expect from a 800 nm soliton (120 nm). The DW breaks quickly into two, labeled DW1 and DW2, and following this soliton fission occurs resulting in 4 solitons, and this is the situation at the start of the tapering section.

If the fiber is not tapered the UV DWs would have a slower group velocity than the soliton, and because the gas is not Raman active no red-shifting and consequently no slowing-down of the solitons occurs. Therefore the solitons would never encounter the DWs again. However, in the tapering section the IR solitons are decelerated, and will therefore collide with the leading edge of the UV DWs, and thereby excite a non-degenerate FWM conversion deeper into the UV. Additionally, the increased dispersion and reduced core size in the tapering section facilitates a soliton-DW phase-matching condition further into the UV than with the original core size [26]. During multiple collisions in the tapering section we eventually have generated 2 XUV DWs with 190 nJ of total energy and DW1 centered as far down as 92 nm. As the light propagates in the waist section the propagation losses quickly dampens the UV and IR content, so it is important to propagate as little as possible after the up-conversion has finished. We should here as a practicality mention that we tried to put a reverse taper after the short waist section, and it seems to work quite well to reduce the propagation loss if a longer fiber is needed.

More details into the dynamics can be found by studying the spectrograms, which are shown in Fig. 4 at suitable stages of propagation: The first is right before the start of the taper, $z = 0.17$ m, where two DWs have formed and the soliton fission process has commenced. After propagating 8 cm of the taper ($z = 0.25$ m) the DW2 has been up-converted to the same wavelength as DW1 (140 nm) by soliton collision, and now 3 solitons are seen. After additional 5 cm of propagation ($z = 0.30$ m) the solitons have collided with DW1 and DW2, so they are now up-converted to the XUV. At this stage 4 clear solitons are seen. Finally, at the taper stop ($z = 0.36$ m) DW1 has been up-converted once again to 92 nm due to another soliton collision; its duration is around 8-10 fs. The solitons are now quite weak, which is in turn due to ionization losses just before the taper stop as well as significant propagation losses at the taper waist. Note also that the final major ionization event has blue-shifted the 3. soliton, which is a process that may destroy the soliton.

Already at the early soliton-fission stage ($z = 0.17$ m) the resonances have left significant traces of dispersion delay in the spectrogram, as evidenced by the dotted gray line showing the accumulated dispersion delay $\tau(\omega, z) = [\beta_1(\omega, z) - \beta_1(\omega_0, z = 0)]z$ where $\beta_1(\omega, z)$ is the frequency-dependent inverse group velocity and the z dependence of it indicates that the dispersion changes in the tapering section. It is clear that the resonances are very dispersive, giving rise to quite sharp spectral lines and corresponding long pulses in the spectrogram. This notwithstanding, by comparing with a simulation using the basic capillary MS model without the resonances of the poor-man's model, we find that in the nonlinear dynamics shown here is by and large unaffected by the dispersion of the resonances, while in turn the losses induced by the resonances and the glass material losses play a much larger role. This conclusion is quite sensitive to the resonance strength; in [44] the original impedances used in the perturbative extension of the MS results were found to give inaccurate loss value in the peaks, i.e. at the resonances. The losses

Optics EXPRESS

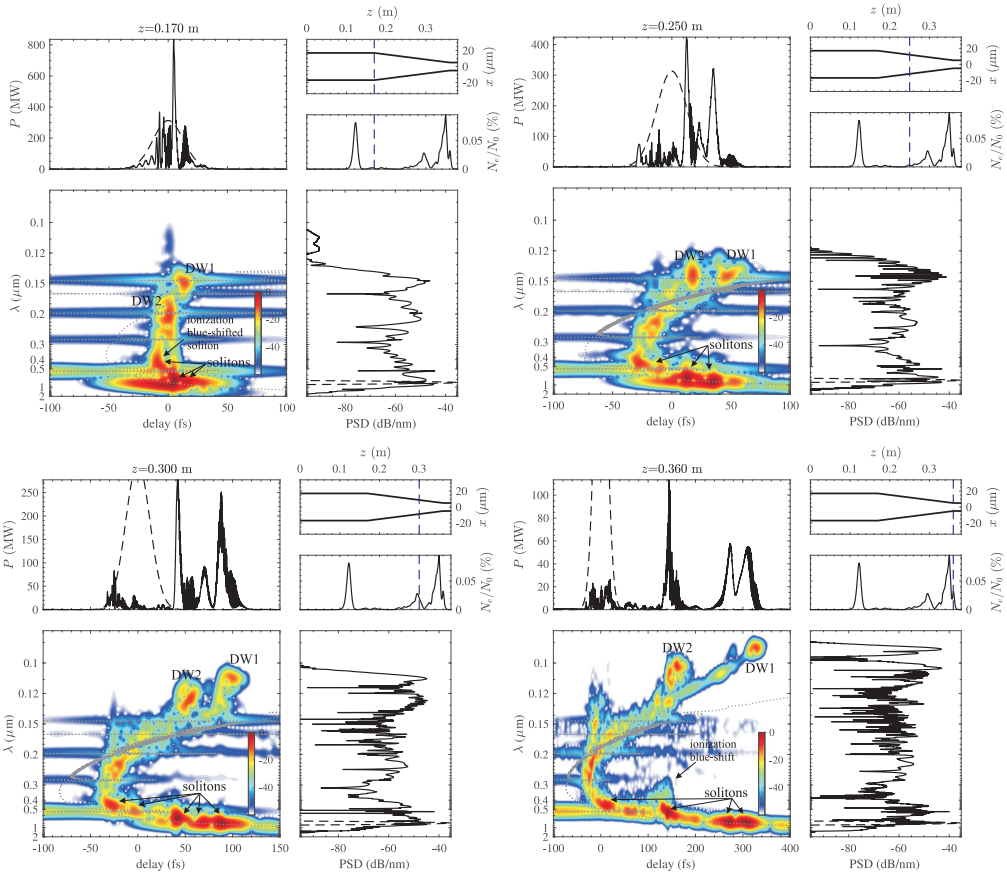

Fig. 4. Spectrograms at selected stages of the simulation in Fig. 3. A 5 fs FWHM gating pulse was used. The dotted gray line shows the accumulated dispersion delay. On top of the spectrogram the power time trace is shown, while to the right the PSD spectrum is shown. In the top-right corner we show in each spectrogram the fiber taper shape and the ionization fraction vs. distance, and the current position is marked with a blue dashed line.

were a factor 4 larger than the BR calculations, and this, in turn, led to much stronger dispersion at the resonance. Essentially the dispersion delay in the resonances is much stronger and this significantly affects the broadband nonlinear interaction.

We investigated in detail the optimal taper shape. It can be made longer and shorter, and be introduced earlier or later in the soliton self-compression dynamics stage. A very short taper quickly decelerates the solitons and gives a short interaction length with the DWs for up-conversion. This limits the efficiency, but it can in certain cases be counter-balanced by a reduced propagation loss in the shorter taper. Starting the taper right at the self-compression stage turned out not to be ideal, most likely because the soliton fission stage is interrupted, and also because in many cases DW2 was not up-converted in the first stage to the same wavelength of DW1. Starting the taper too late leads to a too big delay between the solitons and the DWs and therefore a very long taper is needed to efficiently up-convert. A summary of these points is presented in Fig. 5, which shows variations around the optimized case we have presented so far in the previous simulations (17 cm before the taper, followed by 19 cm taper).

If we start with a fixed taper length (L_T = 19 cm), we see that a very early taper start gives a high overall UV energy, but with limited XUV energy. For pre-taper section shorter than

Optics EXPRESS

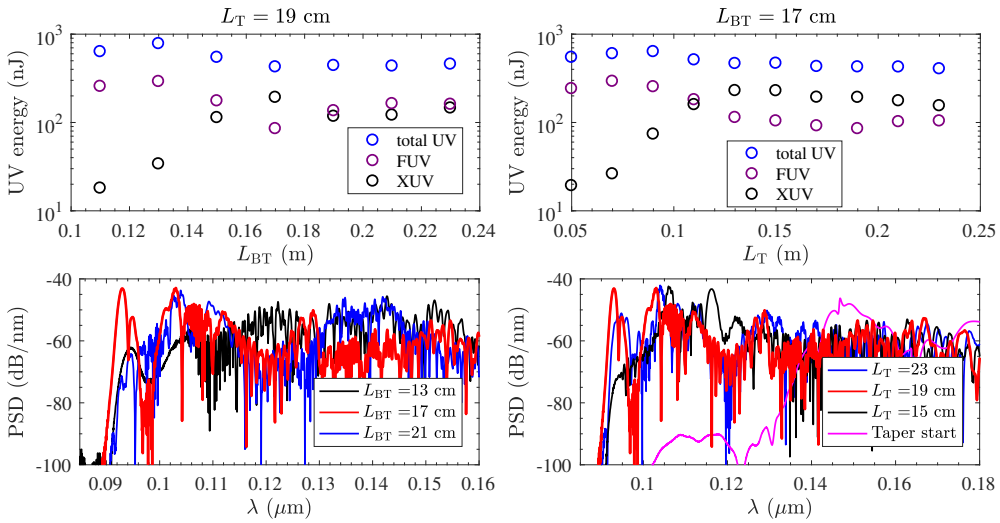

Fig. 5. Top row: UV energies (total as well as the FUV and XUV parts of the UV energy) for two cases: fixed taper length (left) and fixed length before taper (right). The data are shown at the taper end, and do therefore not include propagation in the waist section of the taper. Bottom row: FUV (120-200 nm) and XUV (10-120 nm) part of selected spectra; the red spectra in these plots are the same, namely that of Figs. 3 and 4.

L_{BT} = 13 cm the FUV part has not been converted to the XUV, as the collision of the DWs with the solitons becomes inefficient. In this case, L_{BT} = 17 cm stands out as the maximum XUV energy, and looking at the spectra we see that this case has the sub-100 nm DW while the very early and very late taper start do not.

For a fixed length before the taper (L_{BT} = 17 cm), we see the same trend: a very short taper gives only little XUV energy, while above 10 cm taper length the XUV yield is high, indicating that the DWs are upconverted. From the energy it does not appear that L_T = 19 cm is the optimal taper length, as the energy peaks at 13-15 cm. However, this does not take into account that only for the very long tapers do we get the sub-100 nm upconversion of DW1. This is seen in the spectra plotted below the energy figure.

Finally, let us show an extreme example where the fiber taper is very short, both in the section before the taper starts and in the taper as such. This case is shown in Fig. 6, and since the taper sets in already after 2 cm, well in advance of the soliton self-compression stage, the result is that the spectrum broadens massively towards the blue during the taper and that at the taper exit a shock front forms at the leading edge. This generates a massive broadening towards the UV, with a peak centered around 105 nm in the XUV. This, unlike the previous soliton-case, is a 1-step conversion to the XUV. The energy is at the taper exit 15 nJ in the XUV. The spectrogram taken at the end of the taper reveals that the dynamics seem quite identical to optical wave-breaking, but we remind that the tapering section does not introduce normal dispersion. On the contrary, strong anomalous dispersion is introduced to the pulse before the soliton can form, so what happens is that the dispersion length is reduced dramatically and GVD slows down the SPM-generated colors on the red side of the pump and pulls them away from the pulse center so the soliton cannot form. Eventually a very short spike forms on the leading edge, converting photons to the XUV. This is in part aided by the massive blue-shift of the pulse center due to ionization.

Optics EXPRESS

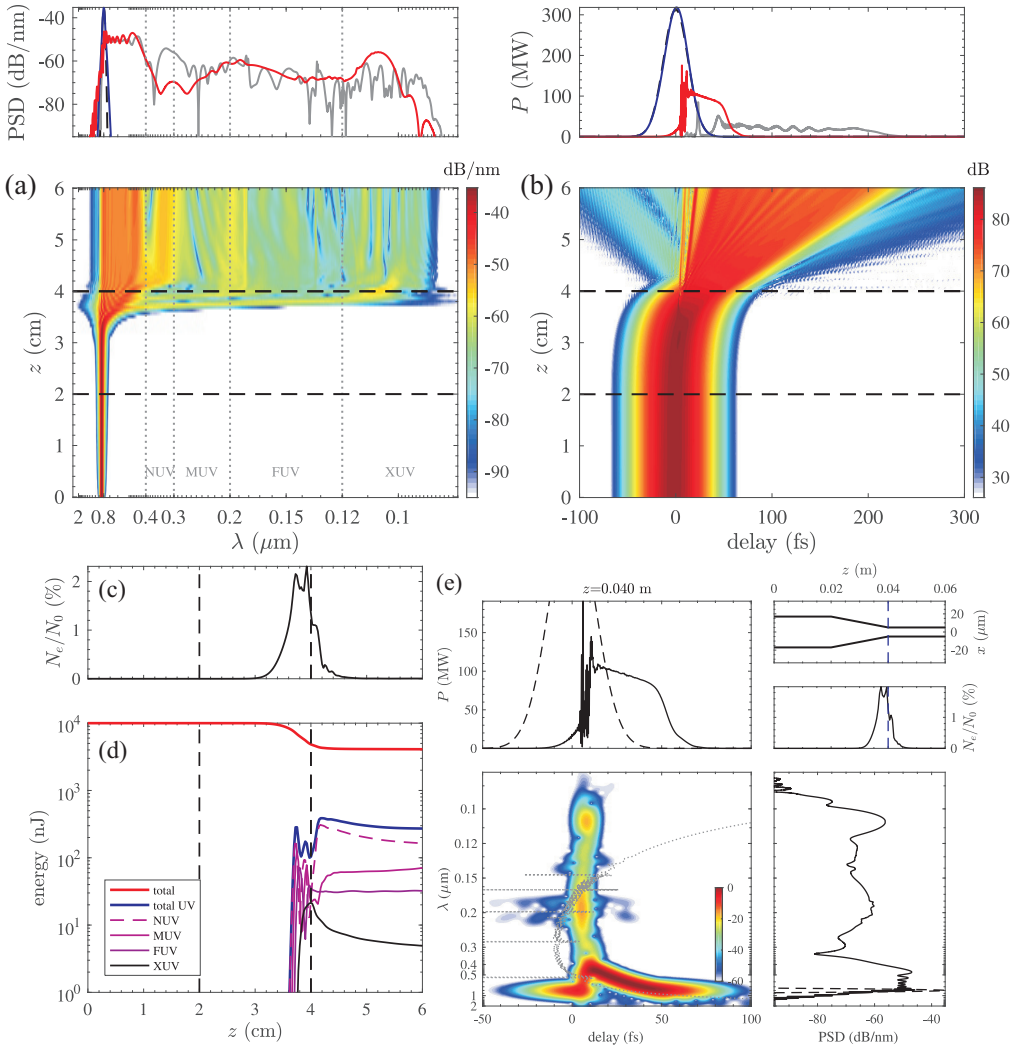

Fig. 6. Simulation of taper from 34 to 10 μm with a short section before the taper (2 cm) and a short taper section (2 cm). The dispersion and loss is as such the same as shown in Fig. 1, only the tapering section is much shorter. Again a 800 nm 30 fs 10 μJ input pulse was used. (a) spectral and (b) temporal evolution vs. distance; (c) ionization fraction and (d) energy distribution vs. distance. (e) spectrogram at the end of the taper.

5. Conclusion

In conclusion we have investigated a new approach to generate XUV coherent pulsed radiation in an HC-AR gas-filled fiber based on soliton-DW dynamics. By tapering a Ne-filled fiber we showed that the solitons could be slowed down to recollide with the UV DWs generated in the untapered stage. This up-converted the far-UV DWs to the extreme-UV, and we found that in this 2-step DW conversion process over 180 nJ of energy could be generated in the 90-120 nm range from 10 μJ 30 fs input at 800 nm. We also showed that a very short taper much before the soliton forms could perform a more traditional direct 1-step DW conversion to the XUV in a process reminiscent of optical wavebreaking, but with an order of magnitude less XUV energy.

Achieving DW generation below 110 nm has not been predicted before, and this we find can

Optics EXPRESS

only be achieved with a tapered fiber. We here used much lower pressures (Ne, 9 bar) than other papers in the literature, which facilitates far- to extreme-UV phase matching of the DW, and reduces ionization losses. It is well known that reducing the fiber core diameter is needed to get XUV phase-matching of the DW, and here we find that the increased propagation losses associated with the smaller cores were mitigated by initially generating the soliton in the untapered fiber and only propagating in smaller cores to achieve XUV DW phase matching for quite short lengths. We found similar dynamics also at lower pressures than 9 bar, but the challenge with lower pressures is to generate the first soliton compression stage in a 10-20 cm fiber without having to use too high pump energies.

The simulations relied on a model recently developed for this purpose [44], where an analytical extension of the capillary model was used to accurately describe the anti-resonant and resonant transmission bands and how they affect the dispersion as well as loss. Importantly, the model also takes into account the lossy nature of glass, which is important in the UV. This analytical extension of the capillary model is a quick way of mimicking complicated and detailed finite-element simulations, so we expect it to find broad usage in the community.

Funding

Innovation Fund Denmark (IFD) (6150-00030A); Danish Research Council (DFF) (4184-00359B and 8022-00091B); United States ARO (W911NF-12-1-0450 and W911NF-17-1-0501).

Acknowledgments

The authors acknowledge fruitful discussions with Michael Frosz, John Travers and Jesper Lægsgaard.

192.38.90.17 {ts '2018-09-10 01:48:19'}